

# Catalysis Science & Technology

Accepted Manuscript

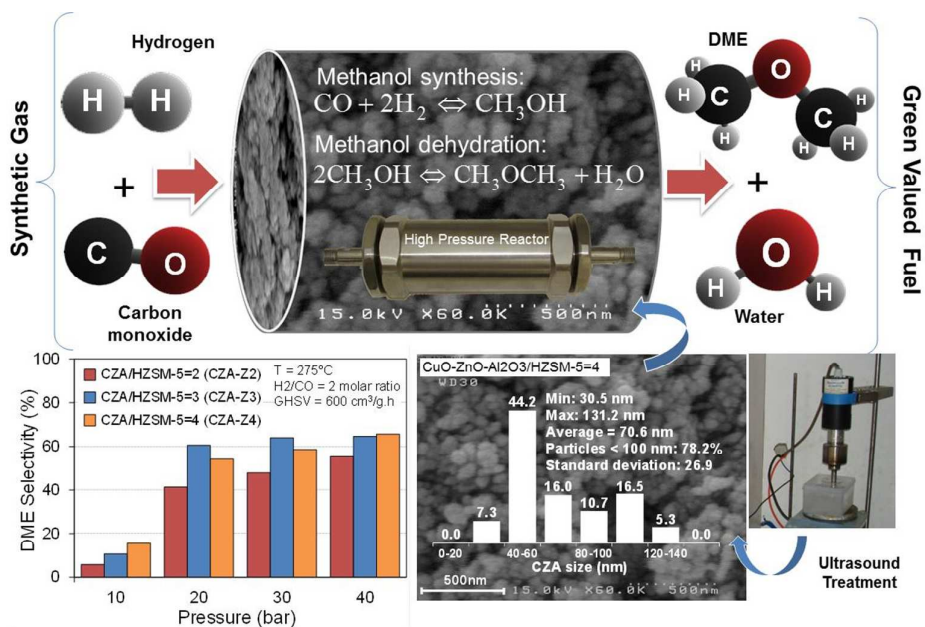


This is an *Accepted Manuscript*, which has been through the Royal Society of Chemistry peer review process and has been accepted for publication.

*Accepted Manuscripts* are published online shortly after acceptance, before technical editing, formatting and proof reading. Using this free service, authors can make their results available to the community, in citable form, before we publish the edited article. We will replace this *Accepted Manuscript* with the edited and formatted *Advance Article* as soon as it is available.

You can find more information about *Accepted Manuscripts* in the [Information for Authors](#).

Please note that technical editing may introduce minor changes to the text and/or graphics, which may alter content. The journal's standard [Terms & Conditions](#) and the [Ethical guidelines](#) still apply. In no event shall the Royal Society of Chemistry be held responsible for any errors or omissions in this *Accepted Manuscript* or any consequences arising from the use of any information it contains.



Hybrid co-precipitation-ultrasound synthesis of CuO-ZnO-Al<sub>2</sub>O<sub>3</sub>/HZSM-5 used in direct conversion of syngas to dimethyl ether as a green fuel

**Direct Conversion of Syngas to Dimethyl Ether as a Green Fuel over Ultrasound-Assisted Synthesized CuO-ZnO-Al<sub>2</sub>O<sub>3</sub>/HZSM-5 Nanocatalyst: Effect of Active Phase Ratio on Physicochemical and Catalytic Properties at Different Process Conditions**

**Reza Khoshbin<sup>1,2</sup>, Mohammad Haghighi<sup>\*,1,2</sup>**

*1. Chemical Engineering Faculty, Sahand University of Technology, P.O.Box 51335-1996, Sahand New Town, Tabriz, Iran.*

*2. Reactor and Catalysis Research Center (RCRC), Sahand University of Technology, P.O.Box 51335-1996, Sahand New Town, Tabriz, Iran.*

---

\* Corresponding author:

Reactor and Catalysis Research Center, Sahand University of Technology, P.O.Box 51335-1996, Sahand New Town, Tabriz, Iran.  
Email: haghighi@sut.ac.ir, Tel: +98-411-3458096& +98-411-3459152, Fax: +98-411-3444355, web: <http://rcrc.sut.ac.ir>

**Abstract**

The effect of active phase (CZA: CuO-ZnO-Al<sub>2</sub>O<sub>3</sub>) to support (HZSM-5) ratio on physicochemical and catalytic properties of CuO-ZnO-Al<sub>2</sub>O<sub>3</sub>/HZSM-5 nanocatalyst for direct conversion of syngas to DME (STD) has been investigated. Nanocatalysts synthesized using a hybrid co-precipitation-ultrasound method in three ratios of CZA/HZSM-5=2, 3 and 4. The surface functional groups, phase evolution, morphology, reducibility and surface area of calcined nanocatalyst were investigated using FTIR, XRD, FESEM, PSD, EDX, H<sub>2</sub>-TPR and BET techniques. It was found that with varying of the CZA content, the physicochemical properties of prepared nanocatalysts changed obviously. The analysis showed that applying ultrasound energy led to uniform coating of HZSM-5 surface by CuO-ZnO-Al<sub>2</sub>O<sub>3</sub>. Moreover, it was found that each catalyst consisted of many small particles whose shapes are almost spherical. H<sub>2</sub>-TPR profiles indicated that reducibility of nanocatalysts was increased with enhancement of CZA ratio. The effect of CZA/HZSM-5 ratio on the catalytic performance was investigated at 200-300°C, 10-40 bar, GHSV=600 to 1500 cm<sup>3</sup>.g/h and H<sub>2</sub>/CO=2. The results showed that the CZA content has great influence on the activity of nanocatalysts and sample with CZA/HZSM-5=4 nanocatalyst showed highest catalytic activity. Furthermore, it was observed that the optimum operating condition for STD reaction is 275°C and 40 bar. The durability of nanocatalyst was investigated during syngas to DME conversion. The nanocatalyst loses negligible activity over the course of reaction.

**Keywords:** ZnO, CuO, Al<sub>2</sub>O<sub>3</sub>, HZSM-5, Co-precipitation, Ultrasound, Syngas, DME.

## 1 Introduction

The possible application fields for DME are diverse and hence, have made it attractive in a long-term perspective [1, 2]. Today, DME is used as an aerosol propellant, a cooking gas, LPG substitute, etc.[3]. In the search for alternative solutions in the transportation fuel field, available and novel technologies are competing in terms of well-to-wheels greenhouse gas emissions and energy use. As a compression ignition engine fuel, DME could offer high efficiency from well to wheels [4]. It is an interesting diesel fuel candidate from several points of view. Its cetane number is very high, which means that the ability to auto ignites is good. No carbon-carbon bonds and high oxygen content (35 wt.%) decrease the tendencies of producing particulates during combustion [5].

The direct synthesis of DME from syngas proceeds through two consecutive reactions: methanol synthesis and methanol dehydration [6-9]. Cu-ZnO-Al<sub>2</sub>O<sub>3</sub> is an expected component in a syngas-to-methanol catalyst and has been widely investigated for this reaction [10]. Solid acid catalysts such as alumina, HZSM-5 and clinoptilolite are reported to be active for dehydration of methanol in DME production [11-13]. Various routes have been employed for CZA production such as co-precipitation, sol-gel preparation, urea-nitrate combustion, impregnation and physically mixing [14-17].

The production of heterogeneous catalysts involves high value-added materials, where processing costs are not always economically limiting. Among preparation methods of nanocatalysts, the sonochemical technique is considered as an efficient method. The ability of ultrasound to create highly reactive surfaces, to improve mixing and to increase mass transport makes it a particularly promising technique to explore for catalyst preparation and activation [18-20]. It can produce homogeneous and dispersed nanoparticles without need for expensive instruments and extreme conditions [18, 21].

The effect of ultrasound waves can be attributed to the generation, growth and collapse of micro bubbles in the solution. If the cavitations takes place close to the surface of the particles, a jet of liquid penetrate inside the bubble perpendicular to the particles surface leading to formation of high velocity micro jet of liquid toward the surface [22-24].

In our previous research, a series of CuO-ZnO-Al<sub>2</sub>O<sub>3</sub>/HZSM-5 nanocatalysts prepared by impregnation, co-precipitation-physically mixing and combined co-precipitation-ultrasound methods and their catalytic activity have been investigated toward direct conversion of syngas to DME. It was found that co-precipitation-ultrasound method afforded higher activity on Cu-ZnO-Al<sub>2</sub>O<sub>3</sub>/HZSM-5 nanocatalysts in comparison to physically mixing and impregnation methods for STD reaction [25]. In bifunctional catalysts, choosing suitable composition of hybrid system is very important [26]. However, it was not found any information about effect of bifunctional catalyst composition synthesized using ultrasound energy on its physicochemical properties and catalytic performance toward direct synthesis of DME from syngas. Therefore, combinations of various ratios of CuO-ZnO-Al<sub>2</sub>O<sub>3</sub> with HZSM-5 have been synthesized using co-precipitation-ultrasound method and have been examined to find out optimum composition of this nanocatalyst for direct conversion of syngas to DME. The physicochemical properties of calcined nanocatalyst were investigated using FTIR, XRD, FESEM, PSD, EDX, H<sub>2</sub>-TPR and BET techniques.

## 2 Materials and Methods

### 2.1 Materials

Analytic grade chemicals of copper nitrate (Cu(NO<sub>3</sub>)<sub>2</sub>·3H<sub>2</sub>O), zinc nitrate (Zn(NO<sub>3</sub>)<sub>2</sub>·3H<sub>2</sub>O), aluminium nitrate (Al(NO<sub>3</sub>)<sub>3</sub>·9H<sub>2</sub>O), sodium carbonate were purchased from Merck and HZSM-5 with Si/Al =56 obtained from Zeochem. Furthermore, distilled water supplied by Kasra used in the experiments. All of them used as received without any further purification.

## 2.2 Nanocatalysts Preparation and Procedures

As shown in Figure 1, nanocatalyst preparation method can be divided into two stages. At the first stage (a), the metal oxide solid mixture was prepared using co-precipitation method. A 1.0 M aqueous solution of metal nitrates ( $[\text{Cu}^{2+}] + [\text{Zn}^{2+}] + [\text{Al}^{3+}] = 1.0 \text{ M}$ ) with molar ratio of Cu:Zn:Al=6:3:1 and 1.0 M aqueous solution of sodium carbonate solution were drop-wise added simultaneously into deionised water at constant PH =  $7.0 \pm 0.2$  and temperature of  $70^\circ\text{C}$  while continuously stirring. After the mixture had been aged for 1 h under stirring at the same temperature, the resulting precipitates were filtered and washed out three times. Ultimately, the solid obtained was dried at  $110^\circ\text{C}$  overnight and then calcined at  $350^\circ\text{C}$  under air flow for 5 h. At this stage CO hydrogenation function of bifunctional nanocatalyst (i.e. CuO-ZnO- $\text{Al}_2\text{O}_3$ ) was prepared. At the second stage (Figure 1b), the synthesized nanocatalyst was loaded over HZSM-5 slurry and treated by pulsed ultrasound probe (Bandelin). The ultrasound irradiation condition was: 90 W for 45 min in which 10 min current pulse time and 0.5 min rest time, in argon atmosphere (Figure 2). The obtained solution was dried at  $110^\circ\text{C}$  for 24 h and then calcined at  $350^\circ\text{C}$  under air flow for 5 h. The TGA analysis in our previous work was shown that  $350^\circ\text{C}$  is suitable temperature for decomposition of volatile compounds of dried cake [27]. The synthesized samples are designated as CZA-Z2, CZA-Z3 and CZA-Z4 for CuO-ZnO- $\text{Al}_2\text{O}_3$ /HZSM5=2, 3 and 4, respectively.

(Figure 1)

(Figure 2)

### 2.3 Nanocatalysts Characterizations

Powder X-ray diffraction (XRD) measurements were performed using a Siemens diffractometer D5000 with a Cu-K $\alpha$  radiation source operating at 40 kV and 30 mA in a scanning range of 5-70° (2 $\theta$ ). The diffraction peaks of the crystalline phase were compared with those of standard compounds reported in the Joint Committee of Powder Diffraction Standards (JCPDS) data base files. The crystal sizes of CuO, ZnO, and HZSM-5 of the calcined nanocatalysts were evaluated from full width at half maximum of the XRD peaks by using Scherrer algorithm. The crystallinity of the prepared samples was calculated using the sum of the areas of the most three intense peaks of specific phase in samples at 2 $\theta$  = 5-70°. The microstructure and morphology was studied by field emission scanning electron microscopy (FESEM, HITACHI S-4160). The surface chemical composition and dispersion of the calcined samples was analysed by energy dispersive X-ray analyser (EDX, Cam Scan MV2300). BET (Brunauer, Emmett, and Teller) surface area analyses were done using Quantachrom CHEMBET apparatus. Furthermore, the reducibility of the nanocatalysts were measured by temperature-programmed reduction of hydrogen (TPR-H<sub>2</sub>) using a BELCAT(Japan) which included an online thermal conductivity detector (TCD). The sample was loaded in a quartz reactor and a flow of 6.5% H<sub>2</sub>/Ar with 50ml/min was passing through the samples while the temperature was raised at a rate of 5°C/min up to 400°C. Finally, for addressing surface functional groups, the nanocatalysts mixed with KBr thoroughly in a mortar while grinding with the pestle. Then Place just enough to cover bottom in pellet die. Place in press and press at 5000-10000 psi. Carefully remove the pressed sample from die and place in the UNICAM 4600 Fourier spectrometer in the range of 400-4000 cm<sup>-1</sup>.

## 2.4 Experimental Setup for Catalytic Performance Test

The effect of a range of operating variables such as reaction temperatures and reactor pressures on the catalytic performance of the catalysts was investigated to identify suitable CZA/ZSM-5 ratio and optimize the operating conditions for the STD process. The typical reaction results are compared with respect to CO conversion and product selectivity.

Catalytic activity was evaluated in a fixed micro-reactor made of stainless steel with an inner diameter of 10 mm with a catalyst of 1.0 g. The reactor configuration is shown schematically in Figure 3. A K-type thermocouple was inserted into the catalyst bed to detect the temperature of reaction along the axial length of the reactor. Therefore, the temperature reported in this paper is actual catalyst bed temperature. The reactor was set inside a conventional furnace and the furnace set point temperature was set adjacent to the outer surface of the reactor. The exit line from the reactor to the gas-sampling valve in GC was heated to prevent condensation of any volatile products. Prior to the reaction, the catalyst was reduced by hydrogen under atmospheric pressure at 250°C for 3 h. After reduction, the synthesis gas was fed into the reactor. Experiments were performed in temperatures ranging from 200 to 300°C and a pressure ranging from 20 to 40 bar. The time on stream for catalyst at each temperature was 90 min. Furthermore, the steady state condition was achieved after 30 min. A mixture of carbon monoxide and hydrogen at a H<sub>2</sub>/CO ratio of 2 was supplied through mass flow controllers (Seven Star) to a pre-heater at 120°C, then to the catalyst bed at the designated reaction temperature. When the operating condition reached the desired set point, it was kept constant for 15 min and the product analysis was carried out. Compositions of feed and effluent gas were monitored by a gas chromatograph (GC Chrom, Teif Gostar Faraz, Iran) equipped with two electrical controlled six-port switching valves, a 1 µl sample loop, a flame ionization detector (FID) and a thermal conductivity detector (TCD). The GC column was packed with a plot U column (Agilent) was used for separation of DME, MeOH,

and CO<sub>2</sub>, and a molecular sieve 5A column (Agilent) was used for separation of H<sub>2</sub>, N<sub>2</sub>, CH<sub>4</sub>, and CO. A portion of the effluent gas, after reducing its flow, was directed to a gas chromatograph apparatus. The effluent gas was analyzed several times with 35-40 min intervals during each experimental run. In order to complete separation of gases in GC columns at the minimum time, an efficient temperature program was employed. The column temperature was increased steadily from 40 to 150°C and remained at that level for 4 min, then dropped to 40°C uniformly in 4 min and kept at this temperature for 10 min. It should be noted that argon was used as a carrier gas.

(Figure 3)

### 3 Results and Discussions

#### 3.1 Nanocatalysts Characterization

##### 3.1.1 XRD Analysis

The XRD spectrum of parent HZSM-5 and nanocatalysts prepared with different content of CZA were shown in Figure 4. It was found that with increasing CZA content in nanocatalysts, the intensity of CuO and ZnO peaks increased obviously. The HZSM-5 showed typical reflection lines at low angles at  $2\theta = 7.93^\circ$  and  $23.15^\circ$  which their diffraction intensity decreased obviously due to the interaction between CZA and HZSM-5 zeolite. However, this result indicates that during nanocatalyst preparation the original crystal structure of the zeolite was not damaged. Moreover, the XRD patterns show two reflections at  $2\theta = 35.6^\circ$  and  $38.9^\circ$ . This result is characteristic of monoclinic phase of CuO (JCPDS 01-080-1268). Furthermore, those peaks at  $2\theta = 31.7^\circ$  and  $36.2^\circ$  are ascribed to hexagonal phase of ZnO (JCPDS 01-076-0704). It is observed that the peaks were the most diffused and the peaks

of CuO and ZnO had overlap. For instance, the peak of ZnO at  $2\theta$  of  $36.2^\circ$  is severely covered by the peak of CuO at  $2\theta$  of  $35.6^\circ$ .

The crystallinity and crystallite sizes of HZSM-5, CuO and ZnO for parent HZSM-5 and calcined nanocatalysts are listed in Table 1. It can be found that the average crystallite size of CuO in all of the samples remained almost constant and are at range of 13.9-13.5 nm. Moreover, average crystallite size of HZSM-5 didn't change during nanocatalyst preparation in three nanocatalysts. On the other hand, it can be seen that the crystallinity of CuO and ZnO sensitively depends on CZA content. It increased from 55 to 134 when the CZA/HZSM-5 ratio increased from 2 to 4; however, crystallinity of HZSM-5 strongly decreased in all samples. Although CuO and ZnO peaks were observed in XRD patterns, there are no peaks that could be assigned to  $\text{Al}_2\text{O}_3$ . It can be attributed to low content of  $\text{Al}_2\text{O}_3$  and formation of amorphous phase of  $\text{Al}_2\text{O}_3$  that is in good agreement with previous studies [28]. It should be noted that generally,  $\text{ZnAl}_2\text{O}_4$  or  $\text{CuAl}_2\text{O}_4$  formation temperature is higher than this calcination temperature. For instance, Ianos et al. showed that the  $\text{ZnAl}_2\text{O}_4$  formed at  $500^\circ\text{C}$  [29]. Furthermore, Subhan et al. showed that the  $\text{CuO}\cdot\text{ZnO}\cdot\text{ZnAl}_2\text{O}_4$  formed at  $900^\circ\text{C}$  [30]. Moreover, our previous research showed that  $\text{CuAl}_2\text{O}_4$  obtained at  $700^\circ\text{C}$  [31]. Therefore, these spinels couldn't be formed in this calcination temperature.

(Figure 4)

(Table 1)

### 3.1.2 FESEM Analysis

The morphological properties of HZSM-5 and synthesized nanocatalysts were studied by FESEM and results are shown in Figure 5. The FESEM images of the nanocatalysts exhibit similar morphologies for different CZA content. Moreover, each particle consisted of many

small grains whose shapes are almost spherical. The HZSM-5 was composed of cubic particles with rough surfaces with the grain size of about 1  $\mu\text{m}$ . On the other hand, the grain size of CuO-ZnO-Al<sub>2</sub>O<sub>3</sub> was much smaller than that of HZSM-5. It can be seen that by applying ultrasound energy, the grains of CuO-ZnO-Al<sub>2</sub>O<sub>3</sub> dispersed on HZSM-5 very well so that the cubic particles of HZSM-5 cannot be observed. In slurry, shockwaves created by homogeneous cavitation can create high velocity inter-particle collisions, with impact speeds of several hundred meters per second. The turbulent flow and shockwaves produced by intense ultrasound can drive metal particles together at sufficiently high speeds to induce effective interaction at the point of collision. The high-velocity inter-particle collisions produced in CZA/HZSM-5 slurries cause homogeneity of particles into surface of zeolite. The comparison of FESEM images reveals that with increasing of CZA content, the quantity of grains on the surface of HZSM-5 increased obviously.

The size distributions of surface particles were determined using Image-J analyzer and were displayed in Figure 6. It can be seen that the majority of particles in CZA-Z2 have a small size around 20-40 nm. Furthermore, it is shown that 94.8% of the nanocatalysts have the size less than 100 nm with relatively narrow size distribution. Using this analysis the average size of particles was estimated to be 46.7 nm. The comparison of the size distribution of nanocatalysts reveals that the average size of nanocatalysts increased more and more with increasing CZA/HZSM-5 ratio and reached 53.11 nm and 70.6 nm, in CZA-Z3 and CZA-Z4, respectively. This ascending trend probably could be due to the aggregation of CZA particles in higher CZA/HZSM-5 ratio.

**(Figure 5)**

**(Figure 6)**

### 3.1.3 EDX Analysis

The EDX analysis of CZA/HZSM-5 nanocatalyst with active phase to support ratio of 4 (CZA-Z4) is illustrated in Figure 7. As can be seen all the materials used in the preparation of CZA-Z4 nanocatalysts (Cu, Zn, Al, and Si) are observed in EDX dot-mapping analysis. As explained in XRD analysis, there are no peaks that could be assigned to  $\text{Al}_2\text{O}_3$ , however this component could be detected in this analysis. EDX analysis shows high dispersion and uniform morphology for Cu, Zn and Al in CZA/HZSM-5 nanocatalyst which is one the effective parameters affecting catalytic performance. Furthermore, the results indicate that over the course of synthesis of samples no impurities were observed.

(Figure 7)

### 3.1.4 BET Analysis

The surface area of synthesized samples was measured by BET technique and the corresponding values are shown in Table 1. It appeared that adding CZA to HZSM-5 zeolite exerted a significant influence on the surface area of HZSM-5 and decreased it from 247 to  $142.7\text{m}^2/\text{g}$ . This can be addressed by plugging the pore structure of HZSM-5 with CZA. A comparison of the surface area of the synthesized nanocatalysts indicated that increasing the CZA/HZSM-5 ratio had negligible effect on the surface area of the nanocatalysts. Therefore, it can be stated that surface area remained almost constant.

### 3.1.5 FTIR Analysis

Figure 8 shows FTIR spectra of parent HZSM-5 and nanocatalysts synthesized via co-precipitation-ultrasound method in different CZA/HZSM-5 ratio. It was found that the FTIR patterns of synthesized nanocatalysts have similar trend in all of samples. The FTIR spectrum

of HZSM-5 shows bands at 455, 555, 805, 1095 and 1235 $\text{cm}^{-1}$ , which are assigned to different vibrations of tetrahedral and framework atoms in HZSM-5 [32]. The ratio of the intensities of bands at 455, 555  $\text{cm}^{-1}$  provides an approximate estimate of the degree of crystallinity of a given zeolite sample [33]. A decrease in this ratio has been observed with loading of CuO-ZnO-Al<sub>2</sub>O<sub>3</sub> nanoparticles on HZSM-5. On the other hand, the broad absorption bands at 3450  $\text{cm}^{-1}$  attributed to the hydroxyl groups, which are extensively hydrogen bonded [34, 35]. The band at ca. 1640  $\text{cm}^{-1}$  is assigned to the bonding vibrational mode of the interlayer water molecules [36-39]. The strongest absorption peak at 1095  $\text{cm}^{-1}$  is assigned to the framework stretching vibration band of Si(Al)-O in tetrahedral Si(Al)O<sub>4</sub> in raw HZSM-5 [40]. The position of this bond remains almost unchanged in all of nanocomposites, indicating that HZSM-5 structure is not destroyed even after it is loaded with CuO-ZnO-Al<sub>2</sub>O<sub>3</sub> nanoparticles. Furthermore, not any characteristic bond was observed for other impurities such as Cu(OH)<sub>2</sub> or Zn(OH)<sub>2</sub> in XRD patterns. These results support and complement the XRD data.

(Figure 8)

### 3.1.6 TPR-H<sub>2</sub> Analysis

Figure 9 shows the reduction behaviour of the CZA/HZSM-5 nanocatalysts. The obtained results show that with increasing CZA content, the nanocatalyst reduction profile and peak position change significantly. For all samples, a broad and rather symmetric reduction peak was observed between 100°C and 250°C, which assigned to the reduction of Cu species. As can be seen in this figure, nanocatalyst reducibility depends on CZA content. Starting from CZA-Z2, a peak appeared around 215°C. With increasing the CZA/HZSM-5 from 2 to 3, the position of the reduction peak was shifted towards lower temperatures by ca. 40°C and

appeared at 175°C. Moreover, in the TPR of CZA-Z4, a peak was observed around 165°C. Obtained results from Figure 9 indicated that the nanocatalyst reducibility (% of reduced copper/ initial amount of copper) of CZA-Z2, CZA-Z3 and CZA-Z4 was 75.58, 82.21 and 85.25%, respectively. As CZA content was increased, amount of copper in catalyst was increased. Consequently, amount of reduced copper was increased.

The number of reducible species corresponding to the amounts of adsorbed hydrogen is estimated by the areas of the TPR curves. The obtained results show that reducibility depends on CZA/HZSM-5 ratio. The desorbed amounts of hydrogen from CZA-Z2, CZA-Z3 and CZA-Z4 were 6.7, 7 and 7.1 mmol·g<sup>-1</sup>, respectively. Therefore, it can be concluded that with increasing CZA content, the reducible species of nanocatalysts increase.

Reduction peak represents the reduction of Cu species. It should be noted that although the reduction of bulk ZnO is thermodynamically feasible at high temperatures, ZnO showed no distinct peak of the reduction up to 350°C [41]. With increasing CZA/HZSM-5 ratio, the CuO crystallinity became larger and the reduction peak moved to lower temperatures. The reduction temperature of the CZA-Z4 is much lower than that of the CZA-Z2. As the XRD results indicate, this phenomenon could be attributed to the much larger CuO crystallinity on the CZA-Z4. A comparison of the TPR profiles of the nanocatalysts leads to a conclusion that the addition of CZA content makes their reducibility more facile.

(Figure 9)

## 3.2 Comparative Performance of Nanocatalysts toward Direct Synthesis of DME

### 3.2.1 Effect of Temperature at Different Active Phase Ratio

Due to the exothermic nature of the STD reactions, temperature is a critical parameter which may limit the efficiency of the reaction in terms of both CO conversion and DME

selectivity. Therefore, the effect of reaction temperature on the activity of the composite nanocatalysts in STD reaction was investigated and results are shown in Figures 10-13.

The effect of reaction temperature on the CO conversion of the nanocatalysts is shown in Figure 10. It was found that in all samples, the catalytic activity changed with increasing reaction temperature. For instance, with increasing temperature from 200 to 275°C, the conversion of CO over the CZA-Z4 enhanced from 18.5 to 64%, whereas, it decreased to 54% when temperature reached 300°C. Similar trend were obtained over the admixed catalysts composed of CuO/ZnO/ $\gamma$ -Al<sub>2</sub>O<sub>3</sub> [42]. Furthermore, comparing the results showed that in each temperature, with increasing CZA/HZSM-5 ratio, the CO conversion increased significantly and in CZA-Z4 reached to its highest value. For instance, as the weight ratio of CZA/HZSM-5 increased from 2 to 4, the conversion of CO increased from 50 to 64% at 275°C. The results show that all nanocatalysts are fairly active for DME synthesis, leading to the high conversion of CO in STD reaction over the composite nanocatalyst.

The synthesis of DME from syngas can be represented by the following overall reactions:



According to results H<sub>2</sub>-TPR analysis, with enhancement of CZA content in the nanocatalysts composition, the reducibility of nanocatalyst increased. Consequently, the rate of methanol synthesis increased. On the other hand, by removing methanol during the dehydration reaction, equilibrium conversion shifted to right-hand side. As a result, the conversion of CO in CZA-Z4 reached to its highest value. The obtained results of the experiments show that in the absence of CO hydrogenation catalyst, no reaction takes place. Therefore, it can be concluded that the parent HZSM-5 has not catalytic activity for direct synthesis of DME.

Furthermore, the low conversion of CO at higher temperatures is due to the thermodynamic restrictions of the exothermic reactions as well as coke formation, which leads to partial loss of catalyst activity. Among the results, 275°C has been selected as the optimum temperature.

Figure 11 represents the DME selectivity values obtained from all nanocatalysts which is prepared by co-precipitation-ultrasound method. It was found that in all of nanocatalysts, the DME selectivity remains constant around 63% in all of temperature range except for the CZA-Z2 which had decreasing trend. Furthermore, the products distribution in all samples indicated the absence of undesirable carbonaceous species (i.e. olefin, methane, etc.). These results were greater than the many previous works. For instance, Moradi et al. showed that DME selectivity in Cu-ZnO/Al<sub>2</sub>O<sub>3</sub> which synthesized with sol-gel method was only 0.72 in 240°C and 40 bar [15]. Furthermore, we were showed that DME selectivity in Cu-ZnO-Al<sub>2</sub>O<sub>3</sub>/ZSM-5 which synthesized with impregnation and Precipitation-physically mixing was 6.52 and 38.71, respectively [25].

The selectivity of CO<sub>2</sub> was investigated with respect to the composition of nanocatalysts, and the results are shown in Figure 12. As mentioned above, carbon dioxide is generated through the water-gas shift reaction (WGS) which is carried out during STD reaction simultaneously. Both reactions are promoted in the presence of catalysts containing copper and zinc oxide [43]. As identified in the literature, methanol dehydration reaction is promoted at high temperature [44, 45]. At low temperature region, methanol dehydration reaction proceeds slowly and low concentrations of water produced. Subsequently, a little amount of carbon dioxide is produced during the WGS reaction. As the temperature increased, methanol dehydration reaction proceeds significantly and higher amount of carbon dioxide was produced. This phenomenon leads to decrease of DME selectivity in CZA-Z2. A comparison of the TPR-H<sub>2</sub> profiles of the nanocatalysts leads to a conclusion that the addition of CZA

content makes their reducibility more facile. This can be attributed to the larger CuO crystallinity and higher dispersion of CZA in high content CZA samples (Figure 6).

For the further confirmation of these suggestions, the selectivity of DME in oxygenate products was investigated with respect to the composition of nanocatalysts, and the results are shown in Figure 13. As can be seen in this figure, the  $S_{\text{DME,O}}$  is not depended on composition of nanocatalyst and remained almost constant over the entire temperature range. In the STD reaction, methanol is observed as an intermediate species for the governing process and is an index to determining of the relative rates of the two reactions. Moreover, as can be seen in Figure 12, the  $\text{CO}_2$  selectivity in CZA-Z3 and CZA-Z4 is not depended on composition of nanocatalyst and remained almost constant over the entire temperature range. These results indicated that when the contribution of CZA in nanocatalyst composition increased, the rate of methanol production over Cu site became higher than the rate of WGS. Furthermore, it was found that the methanol selectivity was very low. For instance, the methanol selectivity in 275°C for CZA-Z2, CZA-Z3 and CZA-Z4 was 2.6, 2.65 and 1.94, respectively. This observation suggests that even in sample with high CZA content, there are enough acidic sites for dehydration of methanol which was produced over hydrogenation sites. In other words, the methanol synthesis rate is much lower than methanol dehydration rate. Consequently, it can be concluded that overall STD reaction rate was controlled by the rate of methanol synthesis step.

**(Figure 10)**

**(Figure 11)**

**(Figure 12)**

**(Figure 13)**

### 3.2.2 Effect of Pressure at Different Active Phase Ratio

The effect of pressure on the CO conversion and the DME selectivity are shown in Figures 14 and 15, respectively. Results showed that with increasing pressure, the CO conversion increased uniformly. A comparison of the activity of the nanocatalysts revealed that with increasing pressure from 10 to 30 bar, the CO conversion was not depended on CZA content significantly. However, when the pressure reached to 40 bar, increasing CZA content promoted the CO conversion and CZA-Z4 emerged highest activity. Contrary to CO conversion curve, increasing CZA content improved DME selectivity over entire pressure range investigated and CZA-Z4 is known as the best nanocatalyst. For instance, in CZA-Z4 at 10 bar, the DME selectivity was 15.4% and the CO conversion was only 4%. When pressure increased to 40 bar, the DME selectivity and the CO conversion reached the highest value of 66% and 64%, respectively. These results were greater than the many previous works such as [46, 47]. According to reaction I, as the methanol synthesis reaction is a volume-decreasing reaction, it proceeds to the right-hand side with increasing pressure and the CO conversion increases. Since STD process is a sequential reaction, with increasing CO conversion, methanol and DME production increased (reactions I and II). Furthermore, as CZA content was increased, the methanol production was increased, consequently. These factors had synergetic effect on catalyst increase of activity and  $S_{DME}$  in CZA-Z4 at high pressures.

To investigate the influence of pressure on methanol dehydration step, DME selectivity in oxygenates products was calculated and results were shown in Figure 16. It was found that as pressure increased from 10 to 40 bar, DME selectivity in oxygenates products remained constant around 95%. These results are in line with thermodynamic fundamentals. As the number of moles in both side of methanol dehydration reaction are the same, reaction is not sensitive to pressure.

(Figure 14)

(Figure 15)

(Figure 16)

### 3.2.3 Effect of GHSV

The effect of GHSV on the catalytic performance in the STD reaction is shown in Figure 17. GHSV was changed from 600–1500 ml/g<sub>cat</sub>.h by varying the feed flow rate while other reaction conditions were 275°C, 40 bar and H<sub>2</sub>/CO=2. As depicted in this figure, the CO conversion declined from 64% to 32% when the GHSV increased from 600 to 1500 ml/g<sub>cat</sub>.h, whereas the DME selectivity, the oxygenate selectivity and the DME selectivity in oxygenate products remained constant. For the same amount of nanocatalyst, higher values of space velocity result in a decrease in the contact time of the reactor and this may influence the reaction progress and the nanocatalyst efficiency.

(Figure 17)

### 3.2.4 Time on Stream Performance of Nanocatalysts

Time on stream study over CZA-Z4 was performed at 275°C, 40 bar, GHSV=600 ml/g<sub>cat</sub>.h and H<sub>2</sub>/CO=2 as was shown in Figure 18. The CO conversion over CZA/HZSM-5 has decreasing trend in 1080 min. Furthermore, it was found that S<sub>DME</sub> and S<sub>DME,O</sub> had no change during stability test. It should be noted that at the end of the test, the catalyst turned completely black. In the reaction condition, it was observed that the selectivity of DME was about 63% without any significant change during the entire reaction time. It was reported that the HZSM-5 with high Si/Al ratio is deactivated slowly in methanol to hydrocarbon reaction and that the deposition of carbonaceous residues on HZSM-5 occurs predominantly on its

external surface [48]. As CZA loaded on the external surface of zeolite, CZA was covered by coke and accessibility of methanol synthesis catalyst was limited. These observations indicated that acidic sites of CZA/HZSM-5 was active enough for dehydration of methanol to DME after pass of this time, while hydrogenation function was deactivated due to coke formation on Cu species. These results are in line with the previous observation [49].

(Figure 18)

#### 4 Conclusions

CuO-ZnO-Al<sub>2</sub>O<sub>3</sub>/HZSM-5 nanocatalyst synthesized successfully using a hybrid co-precipitation-ultrasound method in three ratios of CZA/HZSM-5=2, 3 and 4. The crystallite size of CuO-ZnO-Al<sub>2</sub>O<sub>3</sub> has not been influenced significantly by CZA content, while crystallinity has significantly depended on it. FESEM analysis showed that, applying of ultrasound energy led to uniform coating of HZSM-5 surface by CuO-ZnO-Al<sub>2</sub>O<sub>3</sub>. Moreover, it was found that each nanocatalyst consisted of many small particles whose shapes are almost spherical. The obtained results showed that the surface area was not depended on CZA content. TPR-H<sub>2</sub> profiles indicated that reducibility of nanocatalysts increased with enhancement of CZA content. FTIR results showed that HZSM-5 structure was not damaged even after loading CuO-ZnO-Al<sub>2</sub>O<sub>3</sub>.

Results of activity test showed that the optimum value for the composition of CZA/HZSM-5 nanocatalysts was 4:1. The influence of reaction temperature and pressure were investigated in detail confirming that the optimal reaction temperature and pressure for this catalyst was 275°C and 40 bar, respectively. The CO conversion depended on gas hourly space velocity. However, increasing GHSV resulted in only slight variation in the product distribution. The results from durability tests indicated that catalytic stability during reaction is acceptable.

Further studies on the influence of the other parameters in sonochemical technique such as ultrasound power, irradiation time, solution temperature, type of solvent, etc. are considered for the future works.

### **Acknowledgements**

The authors gratefully acknowledge Sahand University of Technology for the financial support of the project as well as Tabriz Refinery Company and Iran Nanotechnology Initiative Council for complementary financial support.

## References

- [1] M. Higo, K. Dowaki, *Applied Energy*, 2010, **87**, 58-67.
- [2] K. Srirangan, L. Akawi, M. Moo-Young, C.P. Chou, *Applied Energy*, 2012, **100**, 172-186.
- [3] C. Arcoumanis, C. Bae, R. Crookes, E. Kinoshita, *Fuel*, 2008, **87**, 1014-1030.
- [4] T.A. Semelsberger, R.L. Borup, H.L. Greene, *Journal of Power Sources*, 2006, **156**, 497-511.
- [5] R.J. Crookes, K.D.H. Bob-Manuel, *Energy Conversion and Management*, 2007, **48**, 2971-2977.
- [6] L. Vafajoo, S.H.A. Afshar, B. Firouzbakht, J. Jacek, T. Jan, Developing a mathematical model for the complete kinetic cycle of direct synthesis of DME from Syngas through the CFD technique, in: *Computer Aided Chemical Engineering*, Elsevier, 2009, pp. 689-694.
- [7] E.S. Yoon, C. Han, C.A.O.d.N. Rita Maria de Brito Alves, Evaristo Chalbaud Biscaia, Jr., A Review of Sustainable Energy - Recent Development and Future Prospects of Dimethyl Ether (DME), in: *Computer Aided Chemical Engineering*, Elsevier, 2009, pp. 169-175.
- [8] W.-H. Chen, B.-J. Lin, H.-M. Lee, M.-H. Huang, *Applied Energy*, 2012, **98**, 92-101.
- [9] H.-J. Chen, C.-W. Fan, C.-S. Yu, *Applied Energy*, 2013, **101**, 449-456.
- [10] R. Yang, X. Yu, Y. Zhang, W. Li, N. Tsubaki, *Fuel*, 2008, **87**, 443-450.
- [11] R. Khoshbin, M. Haghghi, *Journal of Nanoscience and Nanotechnology*, 2013, **13**, 4996-5003.
- [12] K.C. Tokay, T. Dogu, G. Dogu, *Chemical Engineering Journal*, 2012, **184**, 278-285.
- [13] P.S. Sai Prasad, J.W. Bae, S.-H. Kang, Y.-J. Lee, K.-W. Jun, *Fuel Processing Technology*, 2008, **89**, 1281-1286.
- [14] J.W. Bae, S.-H. Kang, Y.-J. Lee, K.-W. Jun, *Applied Catalysis B: Environmental*, 2009, **90**, 426-435.

- [15] G.R. Moradi, S. Nosrati, F. Yaripor, *Catalysis Communications*, 2007, **8**, 598-606.
- [16] D.-s. Wang, Y.-s. Tan, Y.-z. Han, T. Noritatsu, *Journal of Fuel Chemistry and Technology*, 2008, **36**, 171-175.
- [17] R. Khoshbin, M. Haghghi, *Chinese Journal of Inorganic Chemistry*, 2012, **28**, 1967-1978.
- [18] C. Pirola, C.L. Bianchi, A. Di Michele, P. Diodati, D. Boffito, V. Ragaini, *Ultrasonics Sonochemistry*, 2010, **17**, 610-616.
- [19] A. Pérez, M.A. Centeno, J.A. Odriozola, R. Molina, S. Moreno, *Catalysis Today*, 2008, **133-135**, 526-529.
- [20] Y. Vafaeian, M. Haghghi, S. Aghamohammadi, *Energy Conversion and Management*, 2013, **76**, 1093-1103.
- [21] M.S. Ghodrati, M. Haghghi, J.S. Soltan Mohammadzadeh, B. Pourabas, E. Pipelzadeh, *Reaction Kinetics, Mechanisms and Catalysis*, 2011, **104**, 49-60.
- [22] S.H. Banitaba, J. Safari, S.D. Khalili, *Ultrasonics Sonochemistry*, 2013, **20**, 401-407.
- [23] J. Safari, Z. Zarnegar, *Ultrasonics Sonochemistry*, 2013, **20**, 740-746.
- [24] S.R. Shirasath, D.V. Pinjari, P.R. Gogate, S.H. Sonawane, A.B. Pandit, *Ultrasonics Sonochemistry*, 2013, **20**, 277-286.
- [25] R. Khoshbin, M. Haghghi, *Chemical Engineering Research and Design*, 2013, **91**, 1111-1122.
- [26] R. Khoshbin, M. Haghghi, N. Asgari, *Materials Research Bulletin*, 2013, **48**, 767-777.
- [27] R. Khoshbin, M. Haghghi, *Chemistry of solid materials*, 2013, **1**, 1-16.
- [28] L. Wang, D. Fang, X. Huang, S. Zhang, Y. Qi, Z. Liu, *Journal of Natural Gas Chemistry*, 2006, **15**, 38-44.
- [29] R. Ianos, S. Borcanescu, R. Lazau, *Chemical Engineering Journal*, 2014, **240**, 260-263.

- [30] M.A. Subhan, T. Ahmed, R. Awal, R. Makioka, H. Nakata, T.T. Pakkanen, M. Suvanto, B.M. Kim, *Journal of Luminescence*, 2014, **146**, 123-127.
- [31] P. Estifae, M. Haghghi, N. Mohammadi, F. Rahmani, *Ultrasonics Sonochemistry*, 2014, **21**, 1155-1165.
- [32] I. Othman Ali, *Materials Science and Engineering A*, 2007, **459**, 294-302.
- [33] M.A. Ali, B. Brisdon, W.J. Thomas, *Applied Catalysis A: General*, 2003, **252**, 149-162.
- [34] Z. Abbasi, M. Haghghi, E. Fatehifar, N. Rahemi, *Asia-Pacific Journal of Chemical Engineering*, 2012, **7**, 868-876.
- [35] N. Rahemi, M. Haghghi, A.A. Babaluo, M. Fallah Jafari, P. Estifae, *Journal of Nanoscience and Nanotechnology*, 2013, **13**, 4896-4908.
- [36] L. Chen, L. Li, G. Li, *Journal of Alloys and Compounds*, 2008, **464**, 532-536.
- [37] F. Rahmani, M. Haghghi, P. Estifae, *Microporous and Mesoporous Materials*, 2014, **185**, 213-223.
- [38] S. Allahyari, M. Haghghi, A. Ebadi, S. Hosseinzadeh, *Ultrasonics Sonochemistry*, 2014, **21**, 663-673.
- [39] S. Aghamohammadi, M. Haghghi, M. Chorghand, *Materials Research Bulletin*, 2014, **50**, 462-475.
- [40] I.C.L. Barros, V.S. Braga, D.S. Pinto, J.L. de Macedo, G.N.R. Filho, J.A. Dias, S.C.L. Dias, *Microporous and Mesoporous Materials*, 2008, **109**, 485-493.
- [41] T. Shishido, M. Yamamoto, D. Li, Y. Tian, H. Morioka, M. Honda, T. Sano, K. Takehira, *Applied Catalysis A: General*, 2006, **303**, 62-71.
- [42] L. Chateau, J.P. Hindermann, A. Kiennemann, E. Tempesti, *Journal of Molecular Catalysis A: Chemical*, 1996, **107**, 367-378.
- [43] P. Kowalik, W. Prochniak, T. Borowiecki, *Catalysis Today*, 2011, **176**, 144-148.
- [44] D. Liu, C. Yao, J. Zhang, D. Fang, D. Chen, *Fuel*, 2011, **90**, 1738-1742.

- [45] S.D. Kim, S.C. Baek, Y.-J. Lee, K.-W. Jun, M.J. Kim, I.S. Yoo, *Applied Catalysis A: General*, 2006, **309**, 139-143.
- [46] Y. Zhao, J. Chen, J. Zhang, *Journal of Natural Gas Chemistry*, 2007, **16**, 389-392.
- [47] R. Nie, H. Lei, S. Pan, L. Wang, J. Fei, Z. Hou, *Fuel*, 2012, **96**, 419-425.
- [48] K.-Y. Lee, M.-Y. Kang, S.-K. Ihm, *Journal of Physics and Chemistry of Solids*, 2012, **73**, 1542-1545.
- [49] G.R. Moradi, F. Yaripour, P. Vale-Sheyda, *Fuel Processing Technology*, 2010, **91**, 461-468.

## Figures Caption

- Figure 1. Schematic flow chart for preparation steps of CZA/HZSM-5 nanocatalysts synthesized via combined co-precipitation-ultrasound method with different active phase to support ratios. ....26
- Figure 2. Experimental setup for dispersion of CZA over HZSM-5 using ultrasound energy. ....27
- Figure 3. Experimental setup for testing catalytic performance of CZA/HZSM-5 nanocatalysts synthesized via combined co-precipitation-ultrasound method with different active phase to support ratios. ....27
- Figure 4. XRD patterns of (a) HZSM-5 and synthesized CZA/HZSM-5 nanocatalysts with different active phase to support ratios: (b)2, (c) 3 and (d) 4.....28
- Figure 5. FESEM images of (a) HZSM-5 and synthesized CZA/HZSM-5 nanocatalysts with different active phase to support ratios: (b)2, (c) 3 and (d) 4.....29
- Figure 6. Size distribution histogram of synthesized CZA/HZSM-5 nanocatalysts with different active phase to support ratios: (a)2, (b) 3 and (c) 4.....30
- Figure 7. EDX analysis of CZA/HZSM-5 nanocatalyst with active phase to support ratio of 4. ....31
- Figure 8. FTIR spectrum of (a) HZSM-5 and synthesized CZA/HZSM-5 nanocatalysts with different active phase to support ratios: (b) 2, (c) 3 and (d) 4.....32
- Figure 9. TPR-H<sub>2</sub> patterns of synthesized CZA/HZSM-5 nanocatalysts with different active phase to support ratios: (a) 2, (b) 3 and (c) 4. ....33
- Figure 10. Effect of temperature and active phase ratio on CO conversion. ....34
- Figure 11. Effect of temperature and active phase ratio on DME selectivity. ....34
- Figure 12. Effect of temperature and active phase ratio on CO<sub>2</sub> selectivity. ....35

Figure 13. Effect of temperature and active phase ratio on DME selectivity in oxygenates..	35
Figure 14. Effect of pressure and active phase ratio on CO conversion.....	36
Figure 15. Effect of pressure and active phase ratio on DME selectivity.....	36
Figure 16. Effect of pressure and active phase ratio on DME selectivity in oxygenates. ....	37
Figure 17. Effect of GHSV on CO conversion, DME selectivity, oxygenates selectivity and DME selectivity in oxygenates. ....	37
Figure 18. Time on stream behaviour of CZA/HZSM-5 nanocatalyst with active phase loading of 4. ....	38

### Tables Caption

Table 1. Structural properties of CZA/HZSM-5 nanocatalysts synthesized via combined co- precipitation-ultrasound method with different active phase to support ratios.....	26
---	----

## Tables and Figures

**Table 1. Structural properties of CZA/HZSM-5 nanocatalysts synthesized via combined co-precipitation-ultrasound method with different active phase to support ratios.**

Nanocatalyst	Active phase/support (wt/wt)	$S_{\text{BET}}$ (m <sup>2</sup> /g)	Crystallinity <sup>a</sup>			Crystallite size <sup>b</sup> (nm)			
			ZSM-5	CuO-ZnO	Al <sub>2</sub> O <sub>3</sub>	ZSM-5 <sup>c</sup>	CuO <sup>d</sup>	ZnO <sup>e</sup>	Al <sub>2</sub> O <sub>3</sub> <sup>f</sup>
HZSM-5	Support (ZSM-5)	247	241	-	-	18.1	-	-	-
CZA-Z2	2	142.7	14	55	-	17.2	13.9	-	-
CZA-Z3	3	140.3	16	120	-	18.0	13.4	-	-
CZA-Z4	4	138.3	22	134	-	18.3	13.5	-	-

a. Crystallinity: peak area XRD pattern.

b. Crystallite size estimated by Scherre's equation.

c. Crystallite phase: monoclinic (JCPDS: 00-042-0024)

d. Crystallite phase: monoclinic (JCPDS: 01-080-1268)

e. Crystallite phase: hexagonal (JCPDS: 01-076-0704)

f. Crystallite phase: Cubic (JCPDS: 00-004-0880)

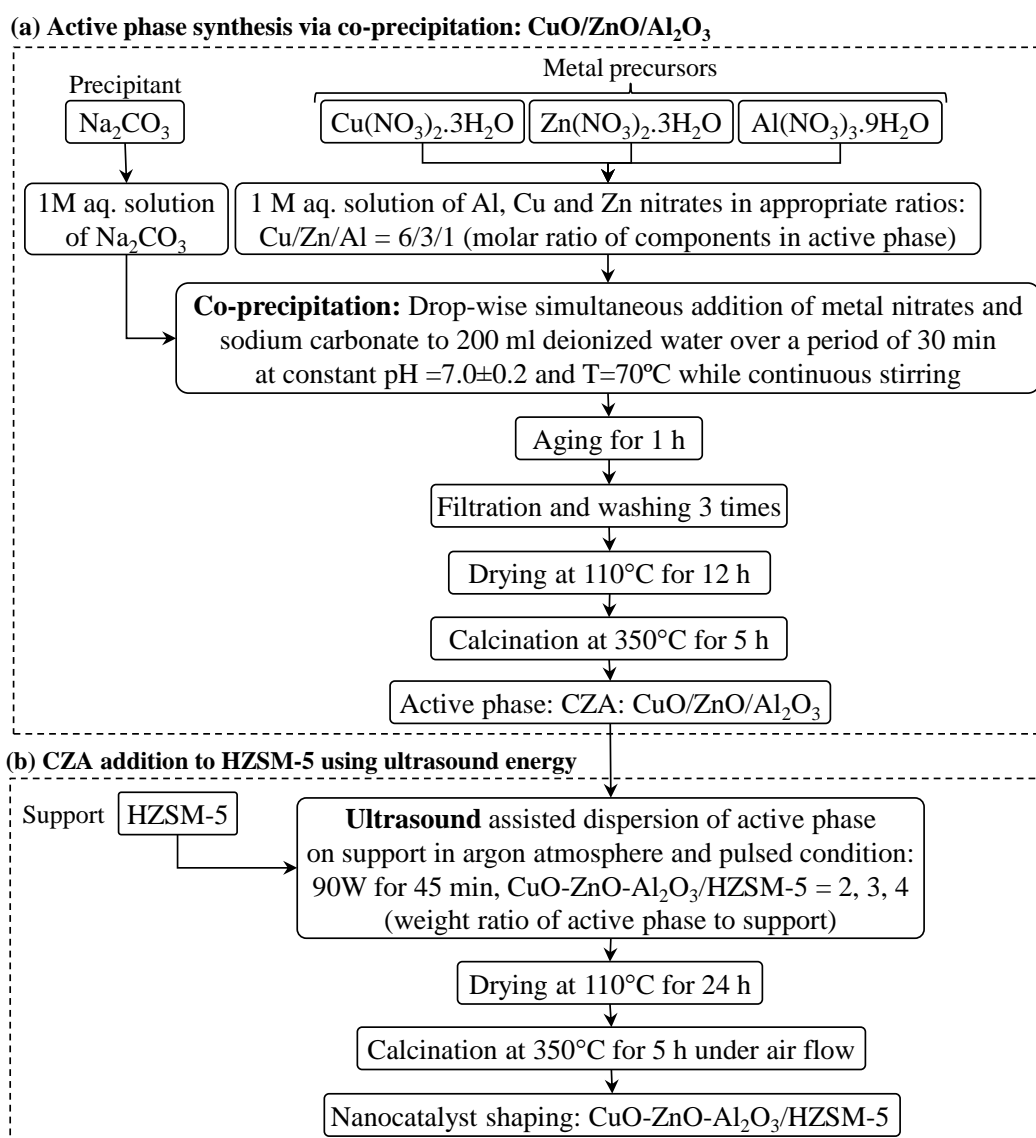


**Figure 1. Schematic flow chart for preparation steps of CZA/HZSM-5 nanocatalysts synthesized via combined co-precipitation-ultrasound method with different active phase to support ratios.**

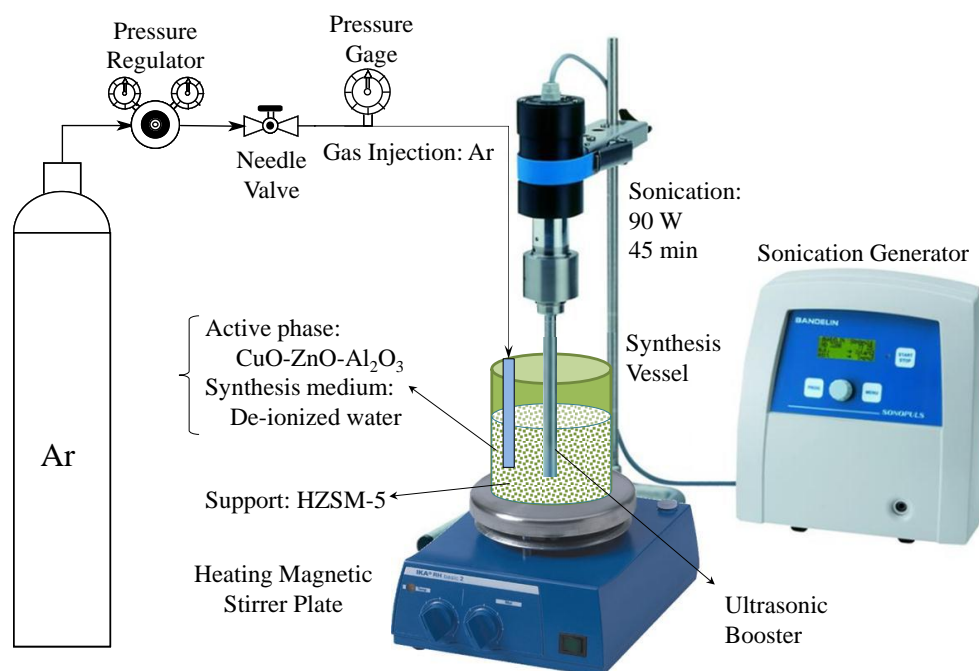


Figure 2. Experimental setup for dispersion of CZA over HZSM-5 using ultrasound energy.

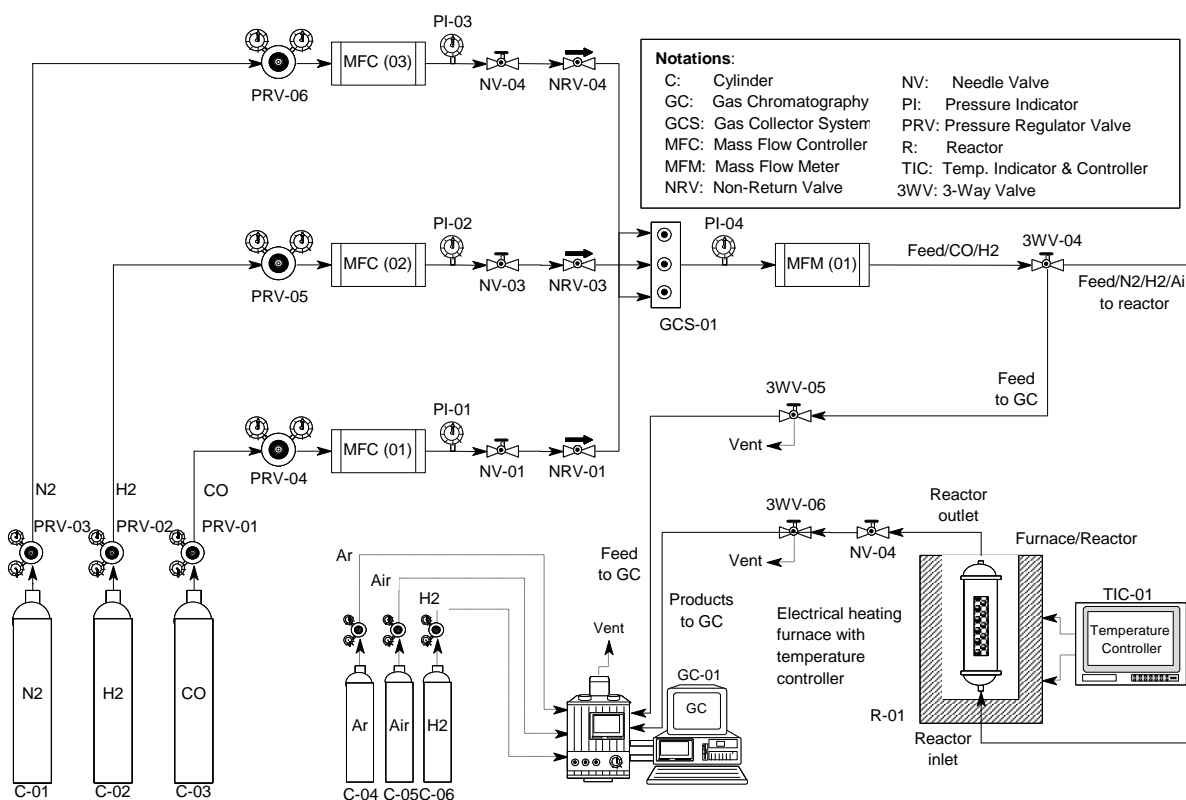


Figure 3. Experimental setup for testing catalytic performance of CZA/HZSM-5 nanocatalysts synthesized via combined co-precipitation-ultrasound method with different active phase to support ratios.

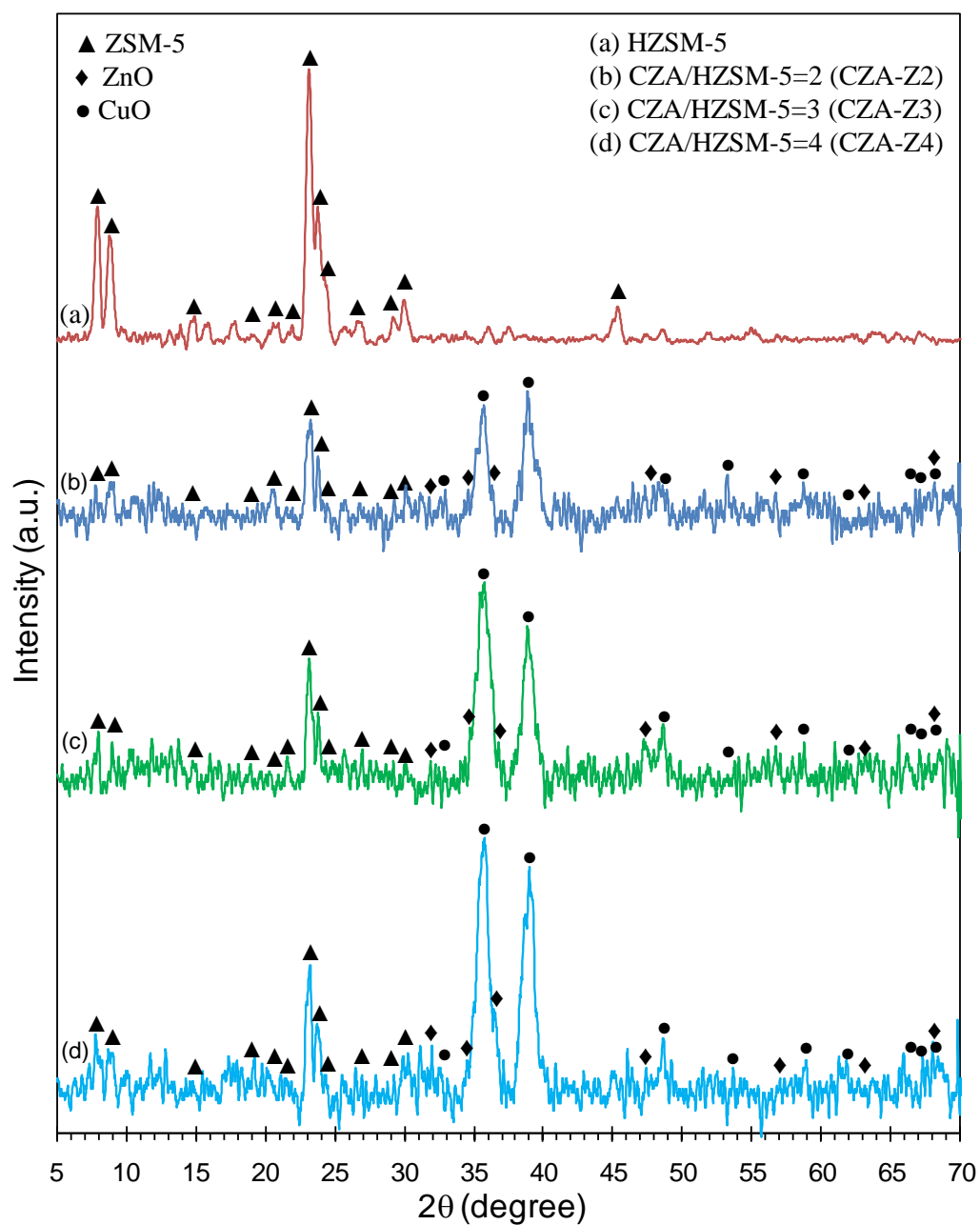


Figure 4. XRD patterns of (a) HZSM-5 and synthesized CZA/HZSM-5 nanocatalysts with different active phase to support ratios: (b) 2, (c) 3 and (d) 4.

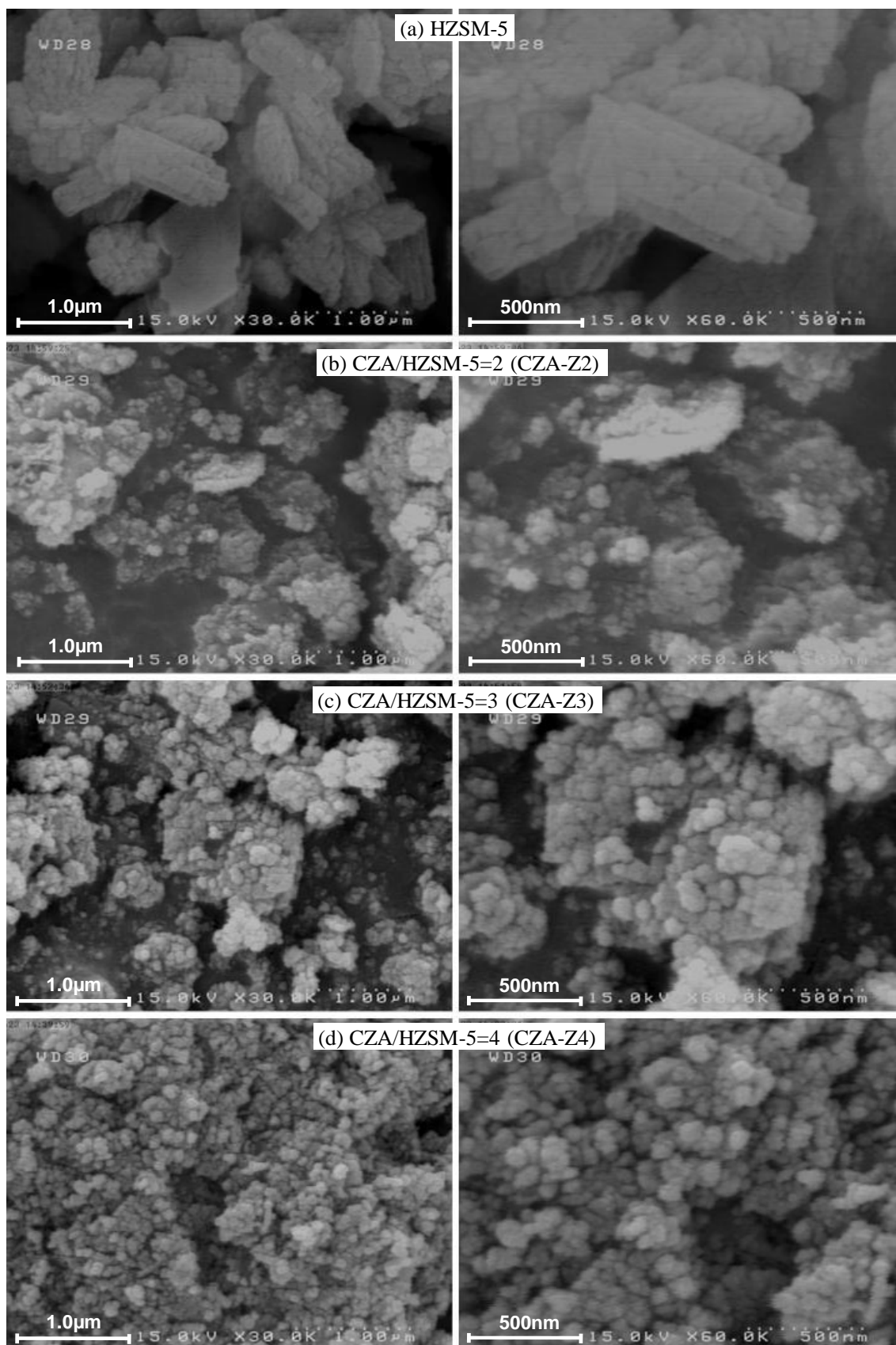
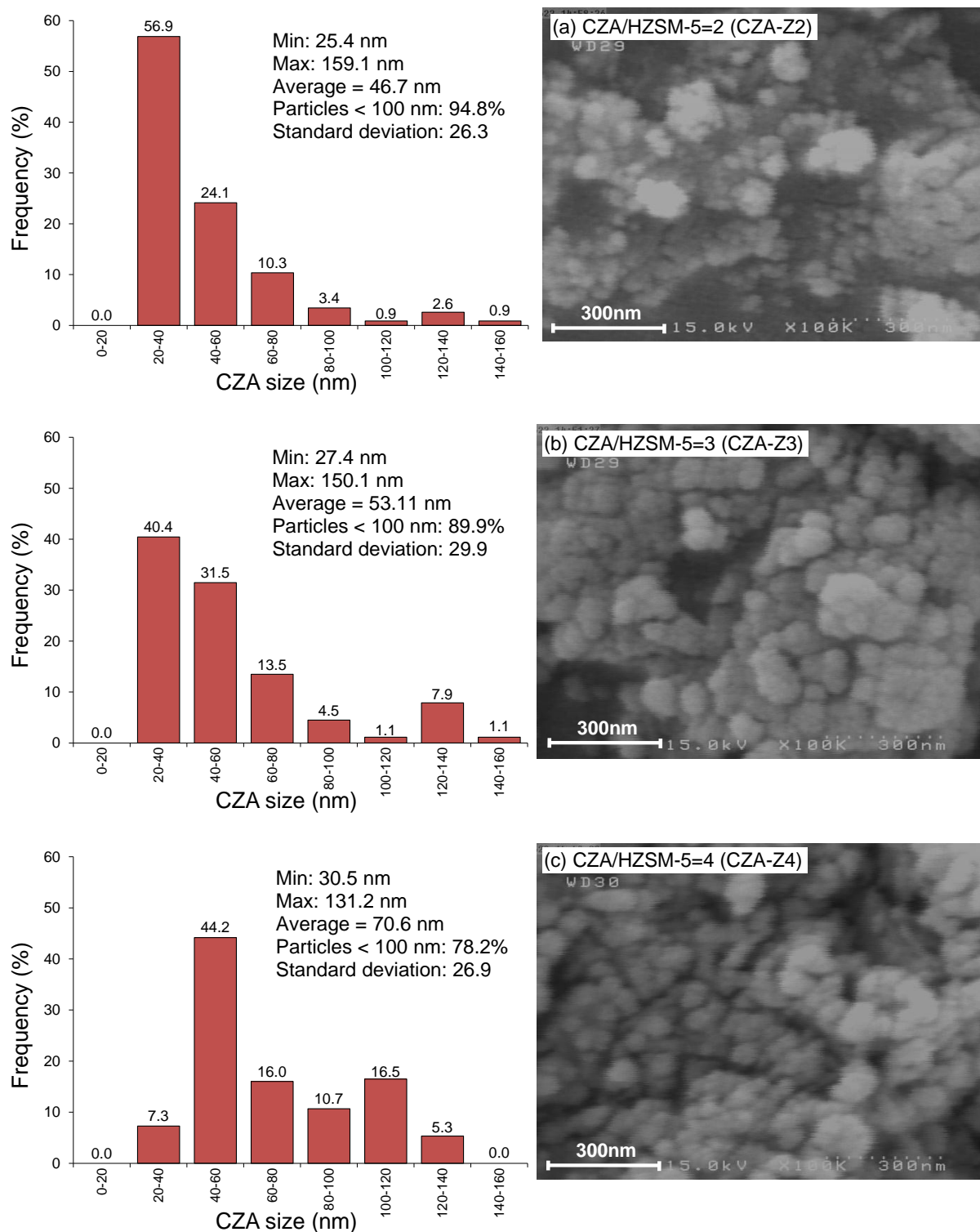


Figure 5. FESEM images of (a) HZSM-5 and synthesized CZA/HZSM-5 nanocatalysts with different active phase to support ratios: (b)2, (c) 3 and (d) 4.



**Figure 6.** Size distribution histogram of synthesized CZA/HZSM-5 nanocatalysts with different active phase to support ratios: (a)2, (b) 3 and (c) 4.

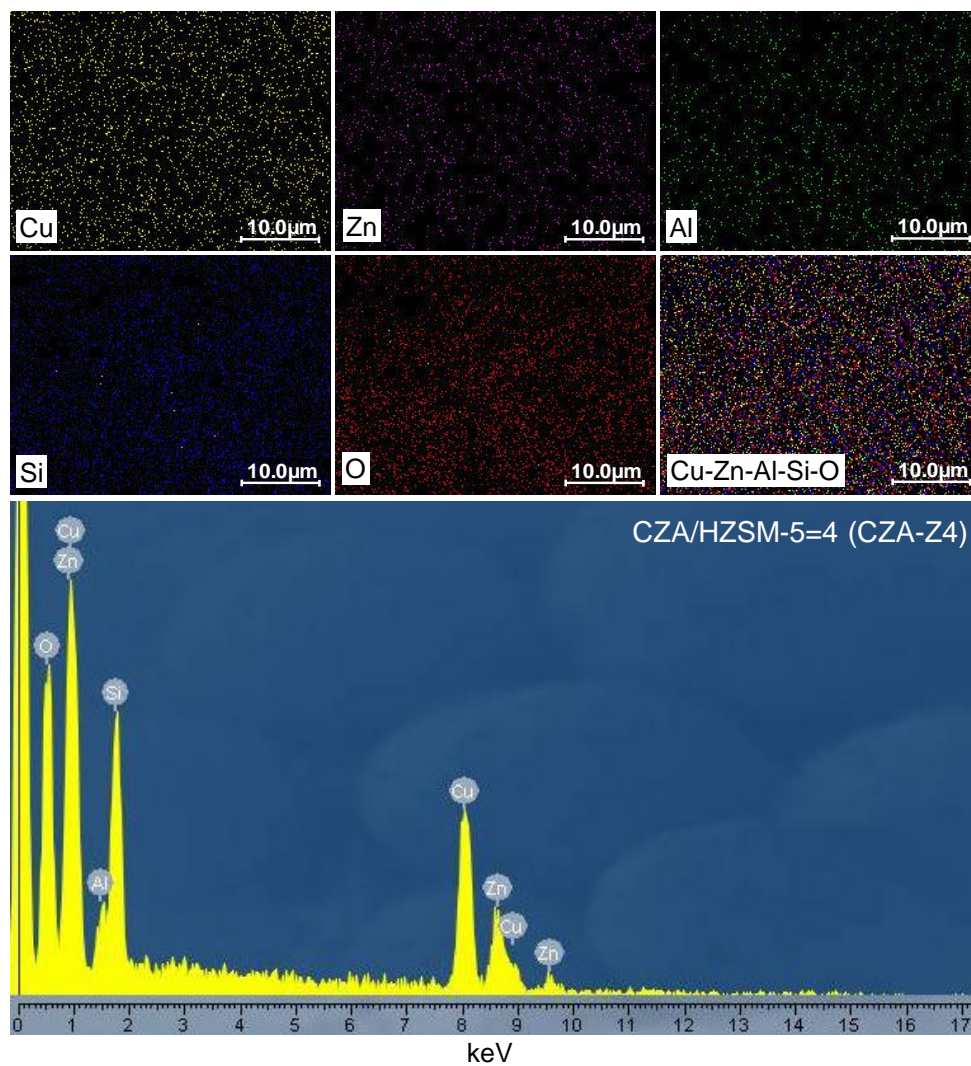


Figure 7.EDX analysis of CZA/HZSM-5 nanocatalyst with active phase to support ratio of 4.

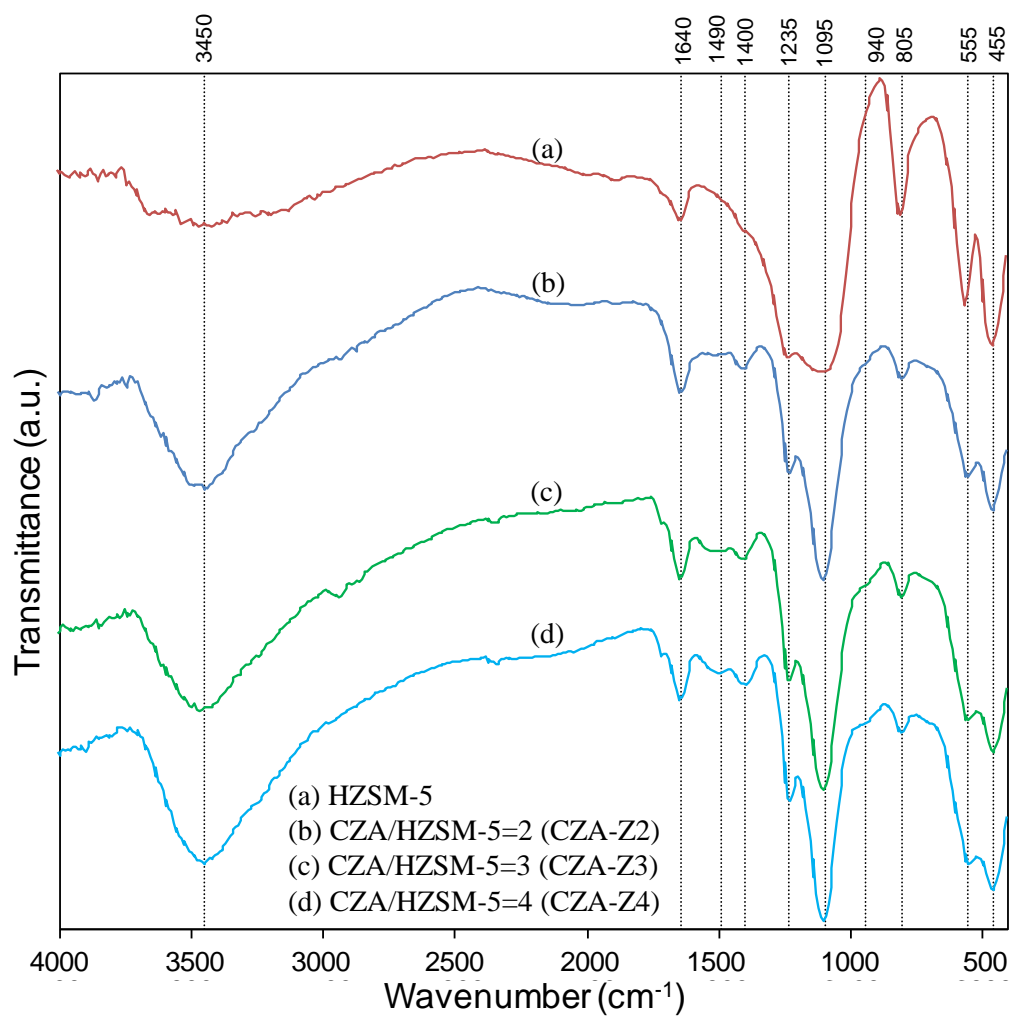


Figure 8. FTIR spectrum of (a) HZSM-5 and synthesized CZA/HZSM-5 nanocatalysts with different active phase to support ratios: (b) 2, (c) 3 and (d) 4.

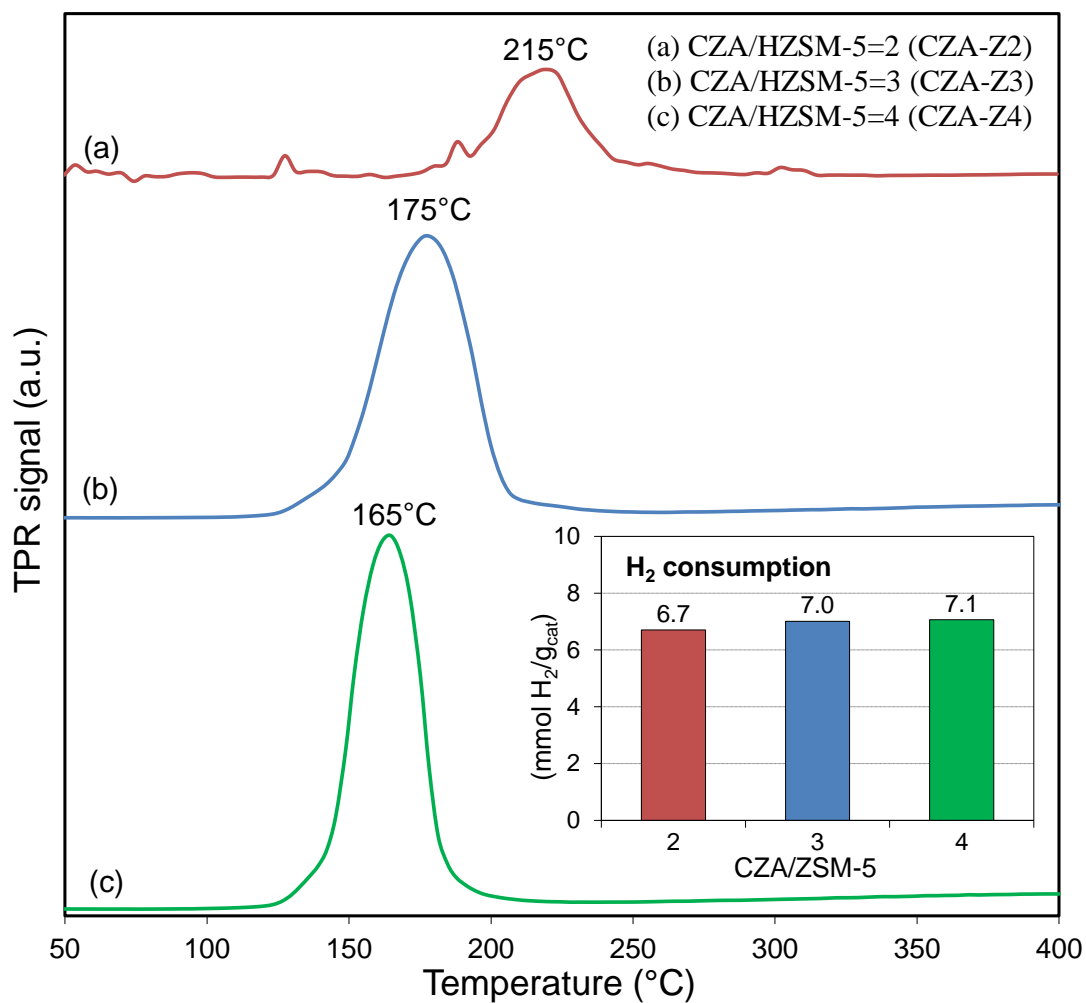


Figure 9. TPR-H<sub>2</sub> patterns of synthesized CZA/HZSM-5 nanocatalysts with different active phase to support ratios: (a) 2, (b) 3 and (c) 4.

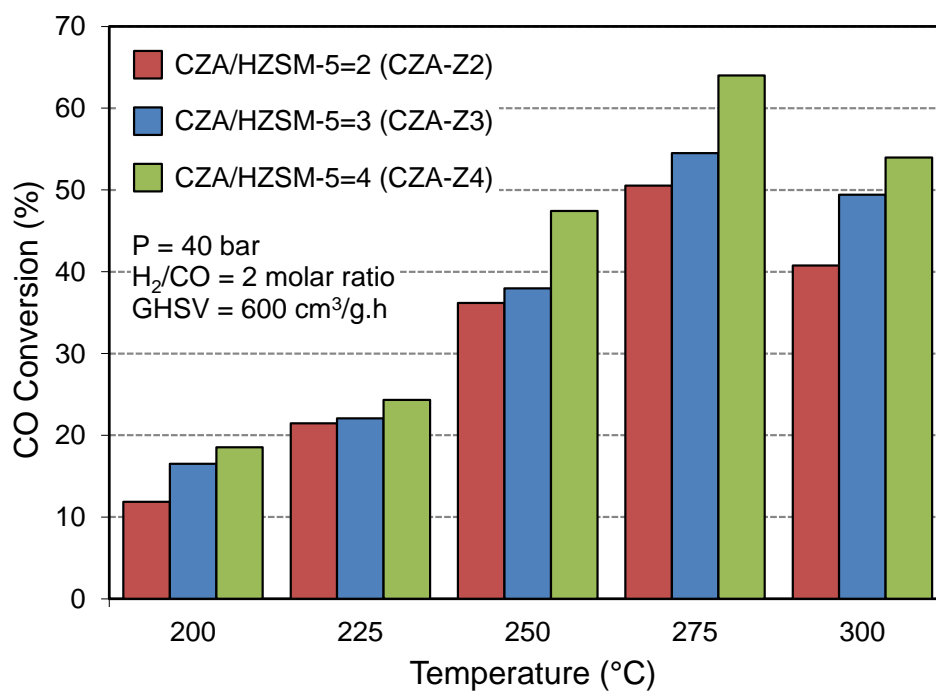


Figure 10. Effect of temperature and active phase ratio on CO conversion.

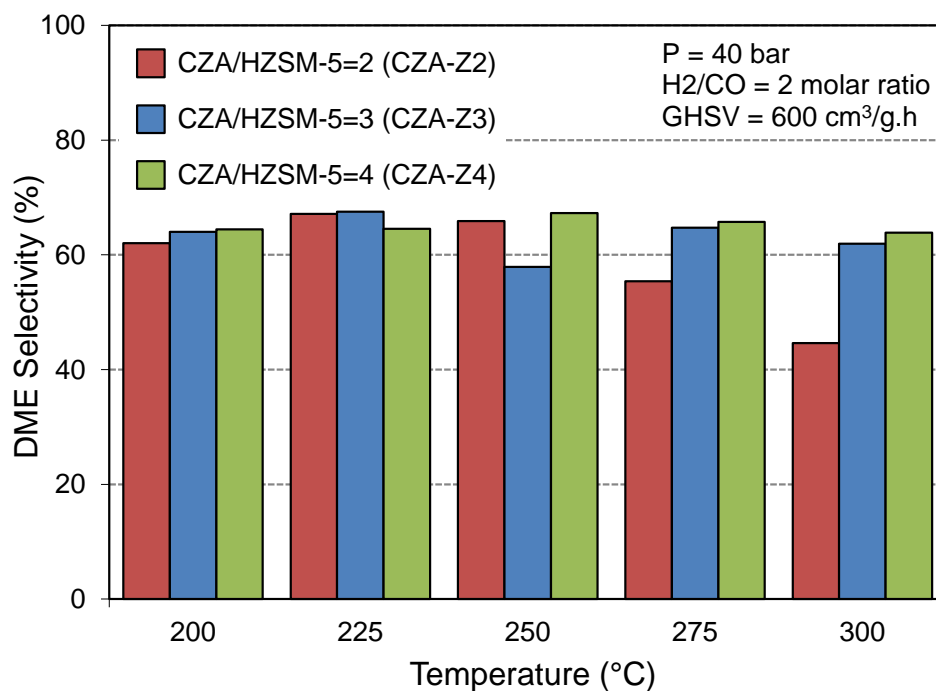


Figure 11. Effect of temperature and active phase ratio on DME selectivity.

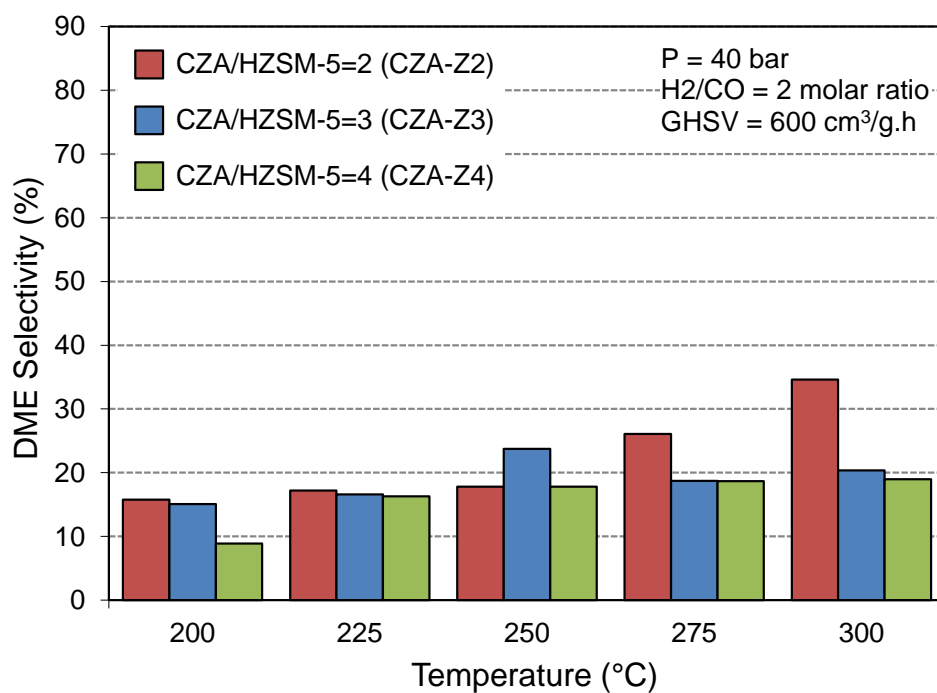


Figure 12. Effect of temperature and active phase ratio on CO<sub>2</sub> selectivity.

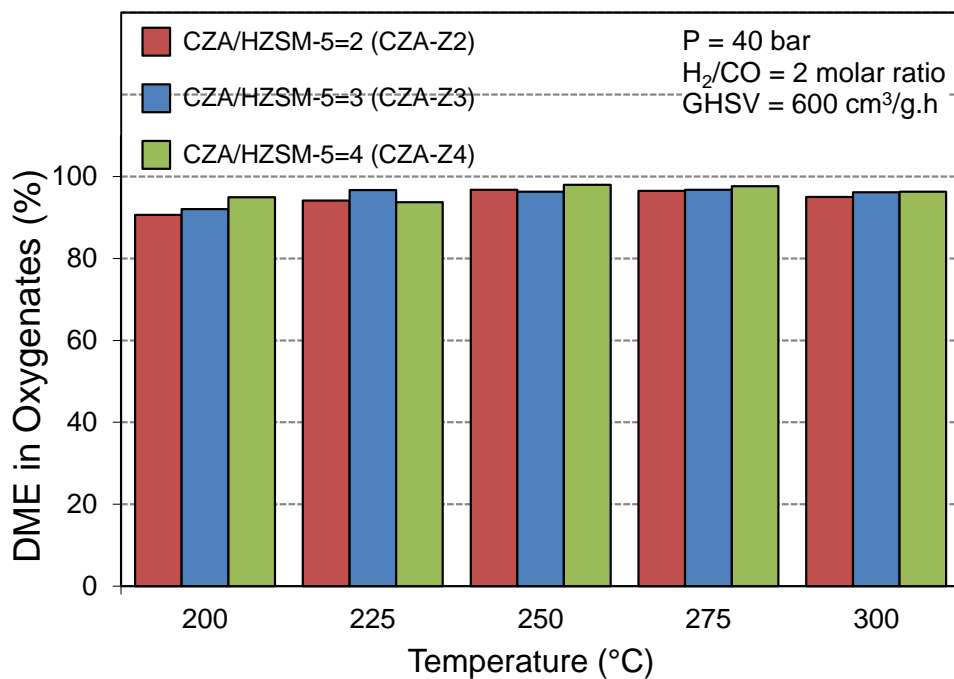


Figure 13. Effect of temperature and active phase ratio on DME selectivity in oxygenates.

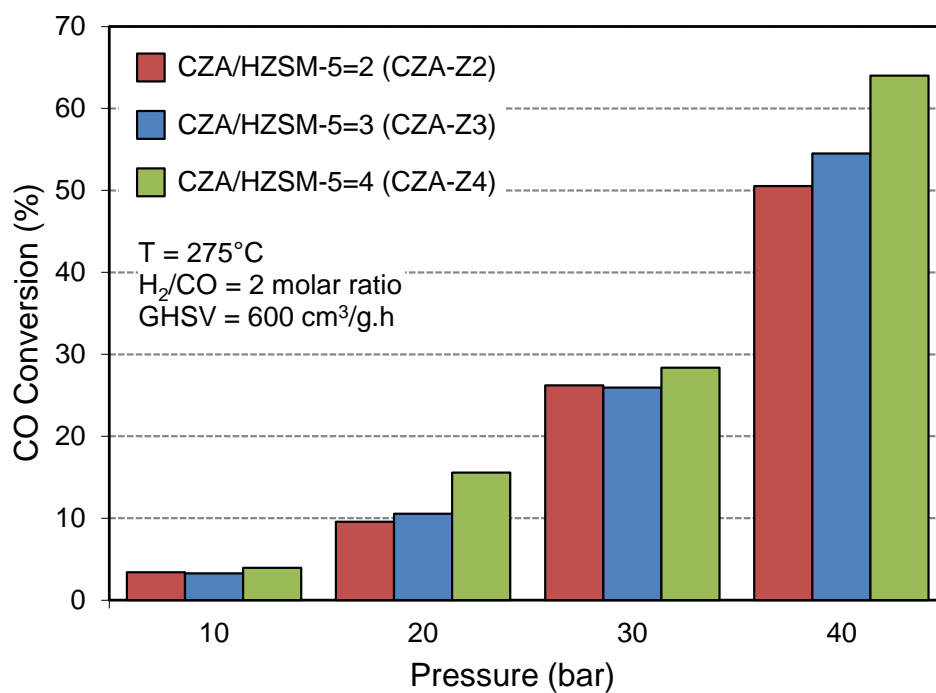


Figure 14. Effect of pressure and active phase ratio on CO conversion.

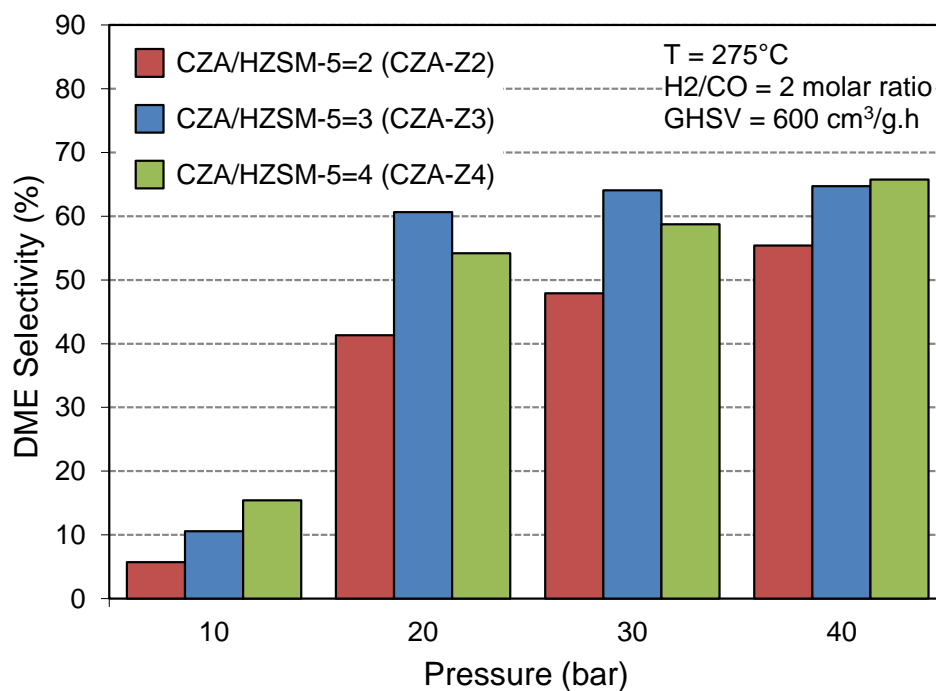


Figure 15. Effect of pressure and active phase ratio on DME selectivity.

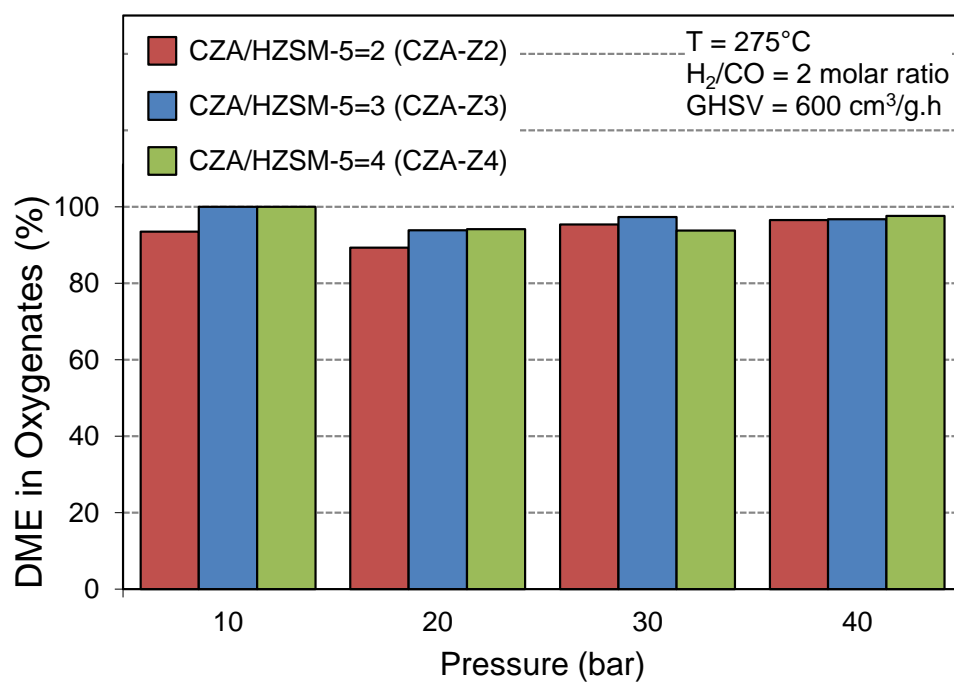


Figure 16. Effect of pressure and active phase ratio on DME selectivity in oxygenates.

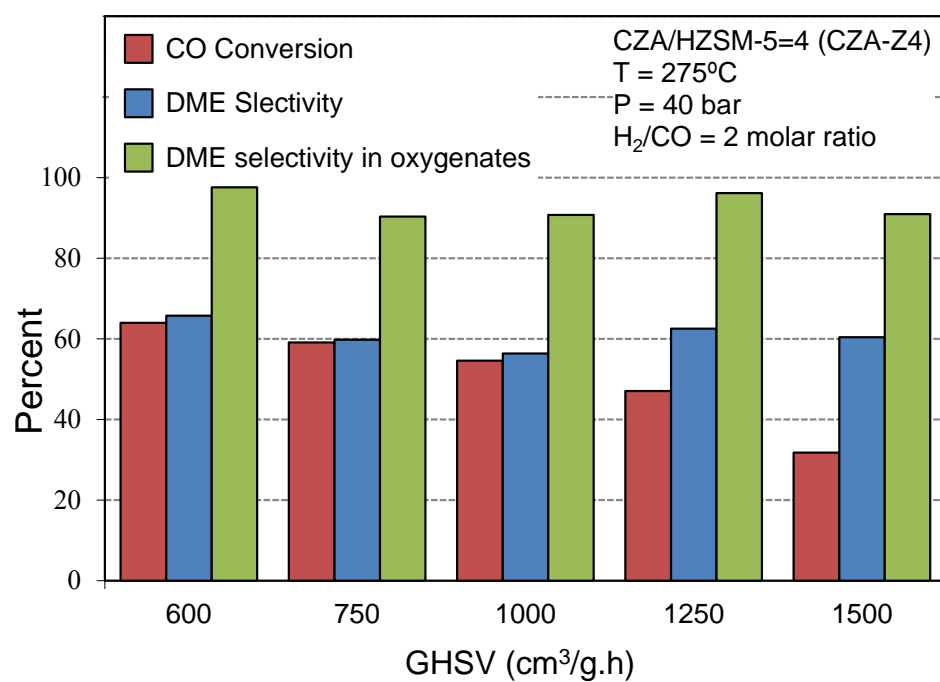


Figure 17. Effect of GHSV on CO conversion, DME selectivity, oxygenates selectivity and DME selectivity in oxygenates.

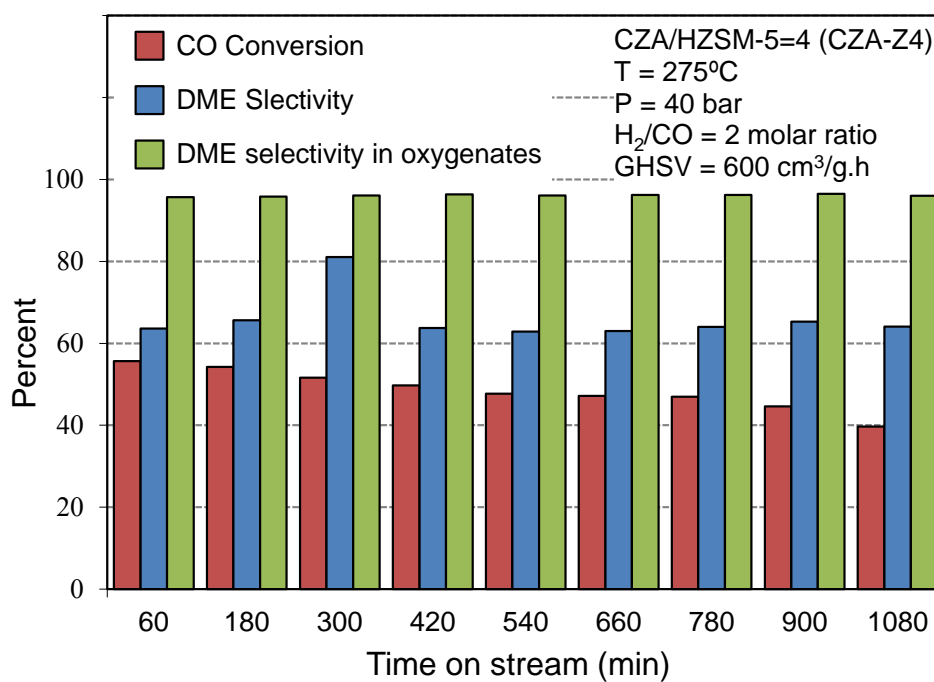


Figure 18. Time on stream behaviour of CZA/HZSM-5 nanocatalyst with active phase loading of 4.